Mud Volcano Imaging using Ambient Seismic Noise

by

Chet Goerzen

A Thesis Submitted in Partial Fulfillment of the
Requirements of the

HONOURS PROGRAM

in the School of Earth and Ocean Sciences

Supervisors: Honn Kao and Lucinda Leonard

University of Victoria

We acknowledge and respect the Lək̓ʷəŋən (Songhees and Xʷsepsəm/Esquimalt) Peoples on whose territory the university stands, and the Lək̓ʷəŋən and W̱SÁNEĆ Peoples whose historical relationships with the land continue to this day.

Abstract

Mud volcanoes are a relatively little known geological phenomenon. They are characterized by the extrusion of mud at the earth's surface. Mud volcanoes represent a serious risk to human life and property, and may also play an important role in the natural greenhouse gas cycle. The Waimata Valley region of New Zealand has been known to have several episodes of mud volcanism. A dense array of short-period geophones was deployed in order to study the subsurface structure of this area. Mud volcano eruptions have occurred many times in the past before the array of geophones was deployed. There was also a mud volcano eruption that occurred several months after the geophone array was decommissioned. Ambient noise tomography was employed in order to study the subsurface structure of the mud volcano by creating a 3-D model of shear wave velocity within the area of mud volcanism. Low-velocity zones were observed in regions underlying the known surface expressions of mud volcanism. An area of mud volcanism that had been dormant since 1930 was observed to correspond to a low-velocity region, suggesting that the source of the mud volcano persists long after an eruption. A low-velocity zone was also observed in the area that later hosted a mud volcano eruption. This suggests that areas of potential mud volcanism may be identified by low-velocity zones revealed by ambient noise tomography.

Contents

List of Tables

List of Figures

1 Introduction

The main objective of this thesis was to investigate the subsurface structure of a mud volcano in the Waimata Valley region, New Zealand. Ambient noise tomography was employed to develop a 3-D model of shear wave velocities in the subsurface. Section 1.1 will provide some background about mud volcanism, and Section 1.2 will describe the geological setting and previous information about mud volcanism in the Waimata Valley. Finally, the method of ambient noise tomography will be described in Section 1.3.

1.1 Mud Volcanism

Mud volcanism has been observed at many places throughout the globe (Hovland et al., 1997; Ginsburg et al., 1999; Evans et al., 2007; Rudolph & Manga, 2010; Bell et al., 2019). One of the most dramatic examples of mud volcanism in recent history is Lumpur Sidoarjo (LUSI). The ongoing eruption of the LUSI mud volcano in Indonesia has claimed several lives and displaced tens of thousands of people (Richards, 2011). LUSI started erupting in 2006, and is still erupting to this day. There is considerable controversy surrounding the triggering mechanism of the LUSI mud volcano (Drake, 2020; Sawolo et al., 2009; Tingay et al., 2008). One hypothesis is that the LUSI mud volcano was triggered by a nearby drilling well (Tingay et al., 2008), while other studies hypothesize that LUSI was unlikely to have been triggered by anthropogenic activities (Sawolo et al., 2009). It appears that no clear consensus has been reached on the triggering mechanism of the LUSI mud volcano.

Methane is known to be released from mud volcano eruptions, and may represent a

significant source of greenhouse gases released into the atmosphere (Milkov et al., 2003). Kopf (2002) also suggests that mud volcanism may be a significant component of water flux from the lithosphere to the hydrosphere.

Mud volcanoes are commonly associated with subduction zones (Kopf, 2002), and generally correspond to rapidly deposited Paleocene-Eocene or Upper Cretaceous sedimentary layers (Ridd, 1970). It is important to make the distinction between geothermally driven mud volcanoes, and pressure driven mud volcanoes. Geothermally driven mud volcanoes are warmed by an igneous source, while pressure driven mud volcanoes are driven by the pressure of the source mud formation. There appears to be roughly equal numbers of mud volcanoes located on-shore and off-shore (Kopf, 2002)

1.2 Waimata Valley geologic setting and mud volcanism

The Waimata Valley is located just north of Gisborne, New Zealand. Gisborne is located on the east coast of New Zealand, and is adjacent to the Hikurangi subduction zone, where the Pacific Plate is subducting underneath the Australian Plate (Figure 1). There is geological evidence for at least ten megathrust earthquakes over the past 7000 years (Clark et al., 2019), as well as descriptions of megathrust earthquakes in Māori oral tradition (King et al., 2019). No megathrust earthquakes have been observed along the Hikurangi subduction zone within the period of instrumentation, but it has been estimated by Wallace et al. (2009) that the Hikurangi subduction zone could host a megathrust earthquake as large as MW 8.7.

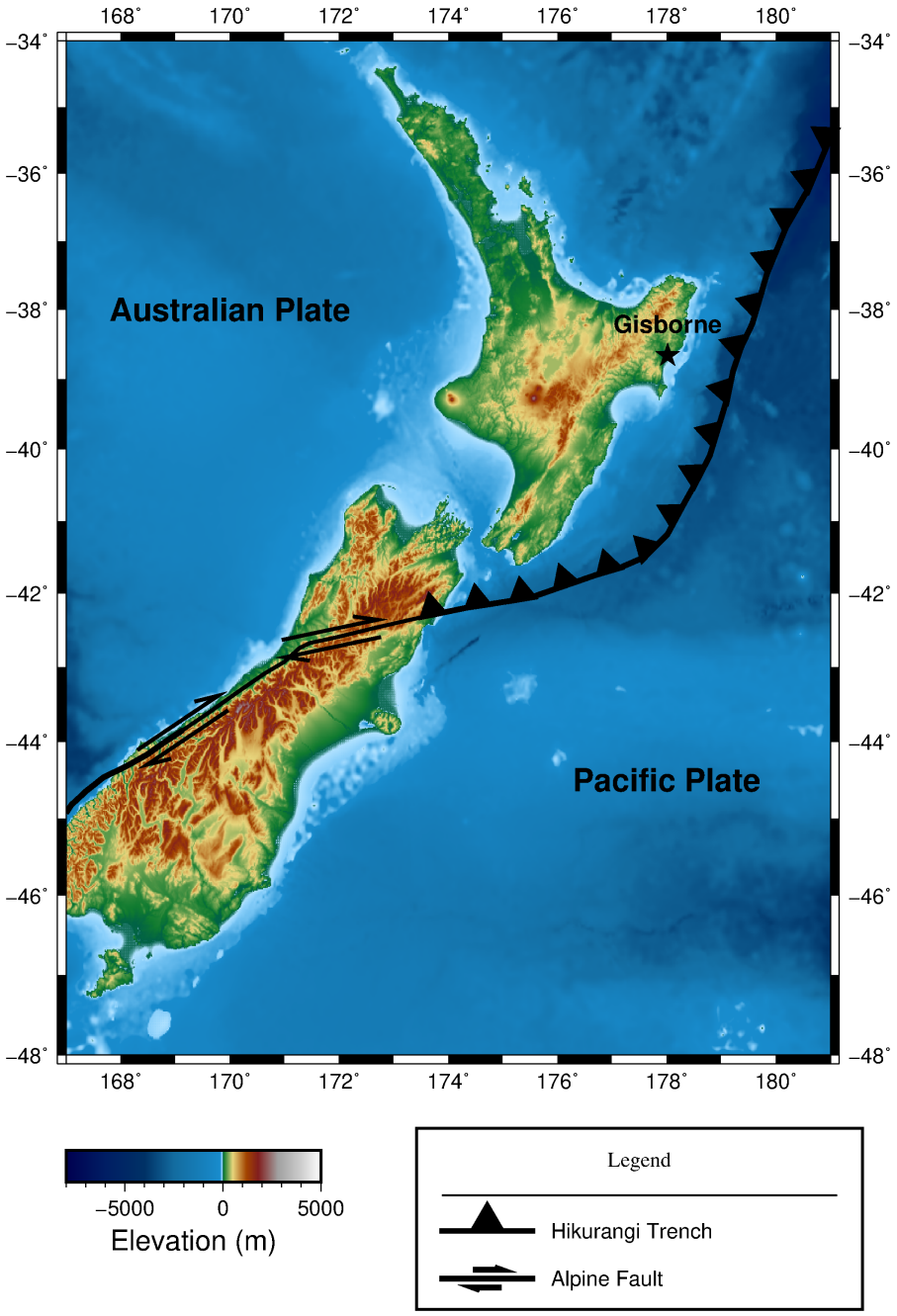

Figure 1: A plot of plate boundaries near the study area.

The Waimata Valley itself is located just north of Gisborne, New Zealand. This area has been of some interest to oil and gas companies (Ridd, 1970; Katz & Wood, 1980), although the Waimata Valley itself was found to be too geologically complex to be economically viable (Ridd, 1964). The area of mud volcanism is characterized by a shift from NE- or NNE-trending faults to a pattern of apparently random synclines and anticlines (Ridd, 1970). The two sites of mud volcanism (labelled "Arakihi Road mud volcano" and "Mangaehu Stream mud volcano" in Figure 2) have been shown to lie on transcurrent faults (Ridd, 1964).

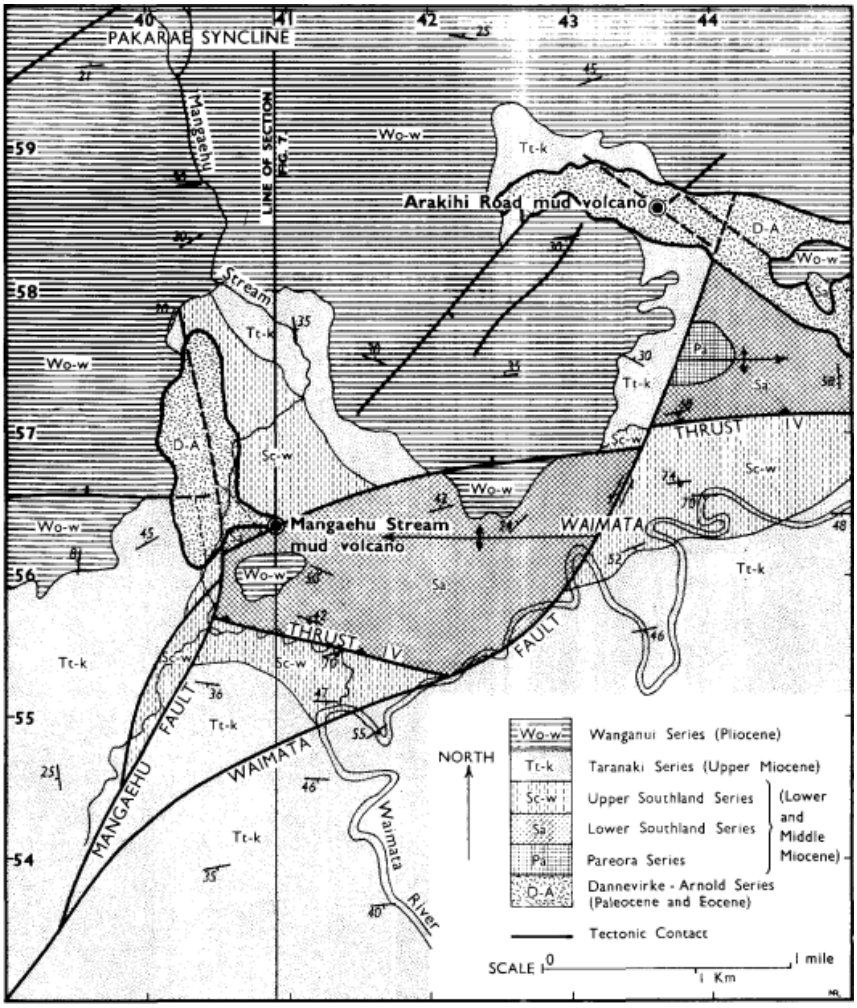

Figure 2: A geological map of the Waimata Valley. Adapted from Ridd (1970). The coordinate system used is the New Zealand 1000 yard grid.

Ridd (1964) has suggested that the Waimata Valley has undergone gravitational gliding, with the interface between plastic bentonites of the Dannevirke-Arnold and the more consolidated Upper Cretaceous formation acting as the decollement.

The Waimata Valley is known to have had two sites of mud volcanism. One eruption site, known as the Mangaehu Stream mud volcano, was reported to have erupted in 1901,

1907, 1908, and 1930 (Ridd, 1970). Eruptions have not been observed at this site since the 1930 eruption. The Mangaehu Stream eruption site is located along an east-west trending high angle fault, which is interpreted to extend to depth (Ridd, 1970). Several large boulders located near the Mangaehu Stream eruption were observed to have striations. Ridd (1970) interpreted these striations to be formed as these boulders rose to the surface through diapiric motion. Analysis of the gas released from the Mangaehu Stream eruption in 1930 found the gas to be predominantly composed of methane, with small components of ethane (Ridd, 1970).

Eruption occurred at a new site in December, 2018, to the north-east of the Mangaehu Stream eruption (Bell et al., 2019). This eruption covered an area of 1.3 hectares over a 5-hour period. The 2018 eruption was observed to be close to areas of previous mud extrusion with previously noted gas bubbling (Bell et al., 2019). Ridd (1970) noted that this area, referred to as the Arakihi Road mud volcano, was characterized by gentle extrusion, as opposed to violent eruptions.

The source mud of the Mangaehu Stream eruption was determined to be from the Dannevirke-Arnold formation, which is composed of bentonitic rock deposited in the Paleocene-Eocene period (Ridd, 1970). The fluids associated with eruptions at both sites were found to be slightly saline (Ridd, 1970; Bell, 2019). In general, mud volcanoes in New Zealand tend to be driven by overpressured mud formations at depth, rather than being geothermally driven (Ridd, 1970). This is certainly the case for mud volcanism in the Waimata Valley.

1.3 Ambient Noise Tomography

Ambient Noise Tomography (ANT) is the method of using background seismic noise to make seismic velocity measurements of the subsurface. This is opposed to earthquake tomography, where the observed arrival times of various seismic phases produced by earthquake rupture are used to measure seismic velocities in the subsurface. Shapiro et al., (2005) were the first to successfully make measurements of the subsurface using the background noise field. It has been shown by Sneider (2004) that the Green's function of a medium between two receivers may be extracted by calculating the cross-correlation of a diffuse wavefield captured by both receivers. This extracted Green's function represents the impulse response of the medium between the receivers. In order to extract the true Green's function from a cross-correlation function, the cross-correlation function must be differentiated in the time domain, and the cross-spectrum must be divided by the squared power spectrum (Sneider, 2004). Note that considerable noise may be added when performing the time domain derivative, and thus simply approximating the Green's function with the cross-correlation function may be a better approach (Sabra et al., 2005). Throughout this thesis, the cross-correlation functions calculated between seismic stations will be referred to as Noise Cross-Correlation Functions (NCFs).

It has been found that the seismic noise field is dominated by surface waves (Haubrich & McCamy, 1969). This implies that the Green's functions extracted from the NCFs are also dominated by surface waves. The seismic noise field has two prominent peaks in the frequency domain, with the primary microseism spanning the period range of 11-20 second, and the secondary microseism spanning the 5-10 second periods (Tian & Ritzwoller, 2015). The secondary microseism is likely due to wave to wave interaction in the deep

ocean, while the primary microseism is likely to be caused by wave to continental shelf interaction in the shallow ocean. The velocity of surface waves is dependent on the period of the waves (Shearer, 2009). This is because the longer period surface waves sample deeper depths than shorter period waves. This period-dependent property of surface waves may be used to extract information about the subsurface structure. In order to extract subsurface information, dispersion curves must be calculated from the NCF's. Dispersion curves are simply the velocity of the surface waves as a function of period. The most commonly used method of extracting the inter-station surface wave dispersion curves is known as Frequency-Time Analysis (FTAN) (Bensen et al., 2007). This will be described further in the Automatic Frequency Time Analysis (AFTAN) section. Given the dispersive nature of surface waves, two different definitions of velocity may be made. The velocity at which energy is transmitted by the wave is known as group velocity, while the velocity of a particular phase is known as phase velocity (Fowler, 2005). Both of these velocities may be used to invert for subsurface seismic velocities. Surface waves are most sensitive to the shear wave velocity of the subsurface, thus subsurface models produced by the inversion of surface wave dispersion curves are best constrained for the shear wave velocity.

There are two main types of inversion methods used for surface wave tomography. The most commonly used method is a two-step inversion. The first step in the two-step inversion is to create a 2-D tomographic map of the phase velocities for each period (Rawlinson & Sambridge, 2005., Barmin et al., 2001). The next step is to extract a 1-D dispersion curve by extracting the node that corresponds to a given geographical location for every period. This dispersion curve can then be inverted for each 1-D model. This yields a 1-D model for each geographical grid node within the study area, providing a pseudo 3-D

model. One of the disadvantages of this technique is that no information from the surrounding grid nodes is used in the inversion of each 1-D model. Because one point of the earth is generally similar to surrounding points, the development of a pseudo 3-D model may not accurately reflect the real earth. Some sort of spatial smoothing may be applied to make the final model more geologically realistic. The other inversion method is a direct inversion. Direct inversions involve only a single step in order to go from the inter-station dispersion curves to the final 3-D model. Some current one-step procedures are outlined in Fang et al. (2015) and Zhang et al. (2018). The benefits of a one-step procedure is increased simplicity, as well as the fact that the inversion intrinsically accounts for relations between geographically close points.

2 Data and Methods

2.1 Data

The seismic data were collected as a part of the NZ3D-FWI project (Bell et al., 2019). In this project, only the data from the area surrounding the mud volcanoes in the Waimata Valley were used. This is known as the Waimata Valley Array (WVA). The WVA consists of 103 three component geophones, of which 97 were used in this study (Figure 3). Each geophone station consists of a DATA-CUBE3 recorder attached to one SM-6/U-B 4.5Hz vertical geophone, and two SM-6/H-B 4.5Hz horizontal geophones (Bell et al., 2019). These geophones have a flat frequency response above 4.5 Hz, and had a sampling rate of 200 Hz throughout the experiment. The instruments were deployed around December 21, 2017, and batteries were inserted at varying periods after that. Batteries were generally

inserted around the end of December 2017. The last instruments were decommissioned on February 12, 2018 (Bell et al., 2017). Some major pre-processing was done to make the data suitable for ambient noise tomography. The data were converted from the CUBE data format into the more standard miniSEED format. The data were then downsampled to 20 Hz, bandpass filtered from 0.01 - 10Hz and converted into daily Adaptable Seismic Data Format (ASDF) (Krischer et al., 2016) files. Only the vertical component geophone recordings were converted to ASDF files, as some of the station orientations were not known. Data from December 21, 2017 to February 11, 2018 were saved to these ASDF files.

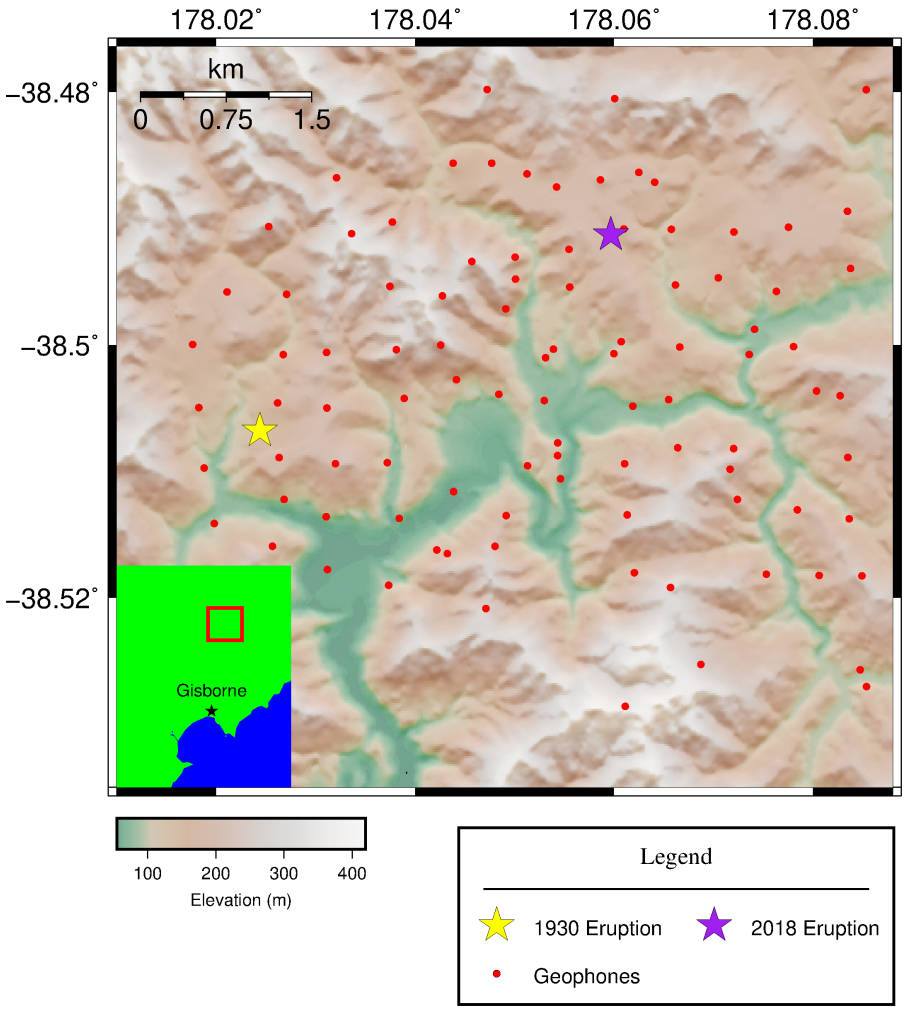

Figure 3: A plot of the study area. Inset plot shows the study area with respect to Gisborne.

In order to characterize the background noise field, frequency-wavenumber beamforming was performed (Rost & Thomas, 2002). Thirty minute segments of data were used for an initial beamforming analysis. Forty-eight of these beamforming analyses were stacked, to reduce the effect of transient events. Only the vertical components of these data were used for the beamforming analysis. The beamforming analysis of the WVA shows that the

noise sources are present at all azimuths (Figure 4).

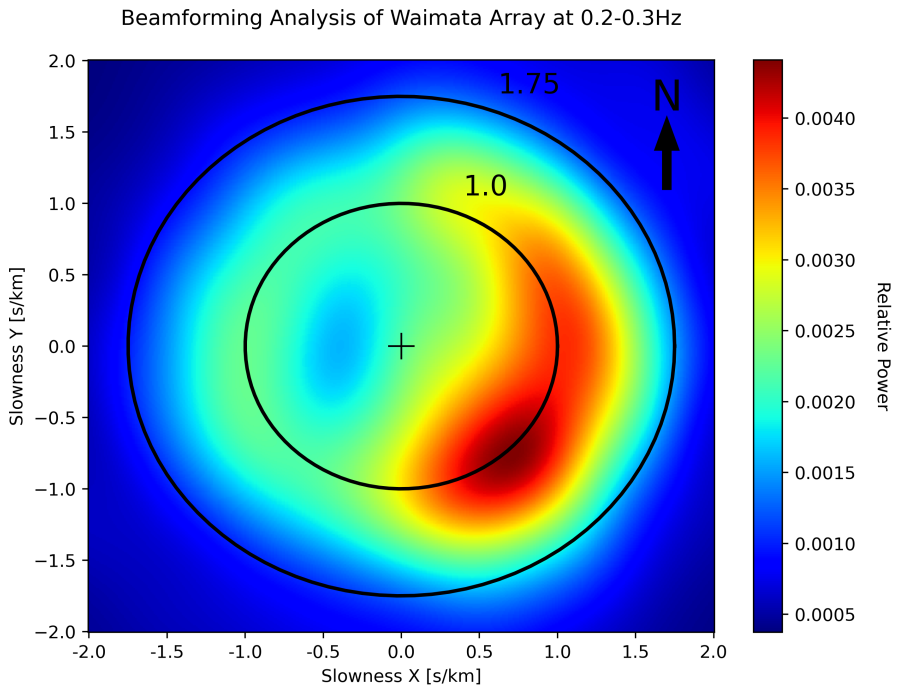

Figure 4: Beamforming analysis of the Waimata Valley array. Note that the greatest power comes from the south-east, which is where the nearest coastline is located.

The strongest noise source appears to be coming from the south-east. This is as expected, because the dominant sources of ambient seismic noise comes from the wave-wave and wave-continental shelf interactions in the ocean, and the nearest coastline to the WVA is to the south-east of the array.

2.2 Cross-correlation

Cross-correlations were calculated using the NoisePy code (Jiang & Denolle, 2020). NoisePy is computationally efficient, performing the cross-correlations in the frequency domain. NoisePy also allows for the use of distributed computing through the mpi4py framework (Dalcin et al., 2005). The instrument response was not removed from the waveforms, as each of the instruments was expected to have an identical instrument response. In order to calculate the cross correlations, a sliding window with a length of 1800 seconds and a step size of 450 seconds was used. This sliding window method is similar to the method of Welch (1967). Seats et al. (2002) have shown that implementing this method significantly increased the signal-to-noise ratio of the NCFs . The trend and mean of each window is removed, and a Tukey window with 5% cosine tapering is applied. No time domain normalization was applied to the waveforms. The NCF's were calculated in the frequency domain by multiplying the complex conjugate of the Fourier transform of the waveform at station A with the Fourier transform of the waveform at station B (Equation 1; Jiang & Denolle, 2020). The maximum cross-correlation lag was 50 seconds.

$$\widehat{C}_{AB}(f) = \widehat{U}_A^*(f)\widehat{U}_B(f) \tag{1}$$

The ambient noise frequency spectrum is not flat, due to the primary and secondary microseisms, as well as other noise sources. As well, the instrument response of any seismic instrument will attenuate frequencies outside of a certain range. For the geophones in this experiment, frequencies below 4.5 Hz are attenuated. In order to make the noise spectrum more broadband, as well as mitigate the effects of transient signals, a procedure called

spectral whitening is applied. This procedure is meant to make the spectral amplitudes of all frequencies more similar, i.e. making the amplitude spectrum that of white noise. This is done by dividing the spectrum by a running mean average in the frequency domain. The window length of the running mean average was 20 samples. Once the running mean average spectral whitening had been performed, the direct-current component (corresponding to the mean in the time domain) was set to zero. Once all the frequency domain processing had been completed, an inverse Fourier transform was performed on the final spectrum, to recover the time domain NCF. An example of a stacked time domain NCF is shown in Figure 5.

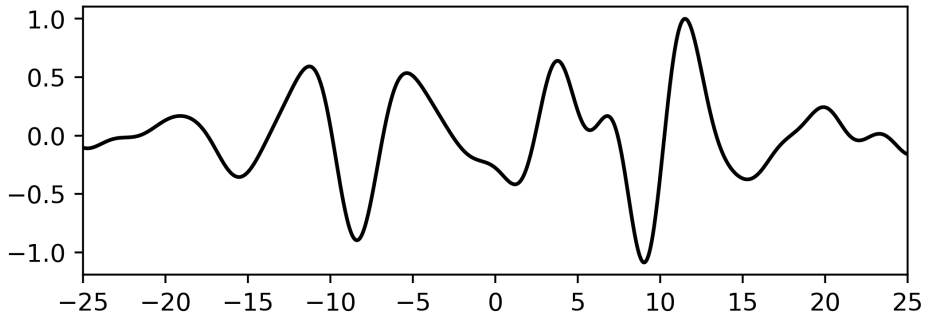

Figure 5: A plot of an individual Noise Correlation Function (NCF). The stations are separated by 6 km. The NCF has been filtered from 0.1-0.3 Hz.

For each station pair, this method produces many individual NCFs over several time periods. Using the parameters in this study, 48 NCFs are produced for each day that both stations in a station pair have data. In order to improve the signal-to-noise ratio of the NCF's, the individual NCF's at each time for a given station pair were stacked to produce a single NCF for each station pair. The stacking method used in this study was a Phase

Weighted Stack (PWS) (Schimmel & Paulssen, 1997). The PWS is advantageous because it amplifies coherent signals, while attenuating incoherent signals. The details described in Schimmel & Paulssen (1997) are outlined in the following. The first step is to calculate the analytic signal of the time series. This is done via the Hilbert transform and is denoted as:

$$\begin{aligned} S_a(t) &= S(t) + iH(S(t)) \\ &= A(t)e^{i\Phi(t)} \end{aligned} \tag{2}$$

where $S(t)$ represents the original time series, $S_a(t)$ is the analytic signal, and $H(S(t))$ is the Hilbert transform of the original signal. $A(t)$ is the amplitude of the signal, and $\Phi(t)$ is the phase of the signal. The PWS is then given by:

$$PWS(t) = \left[\frac{1}{N}\sum_{j=1}^{N} S_j(t)\right] \left|\frac{1}{N}\sum_{k=1}^{N} e^{i\Phi_k(t)}\right| \tag{3}$$

where $S_j(t)$ is the j^{th} and $\Phi_k(t)$ is the phase of the k^{th} signal. In order to show the move-out pattern of surface waves extracted from the NCFs, the stacked NCF from each pair was sorted according to interstation distance and plotted (Figure 6).

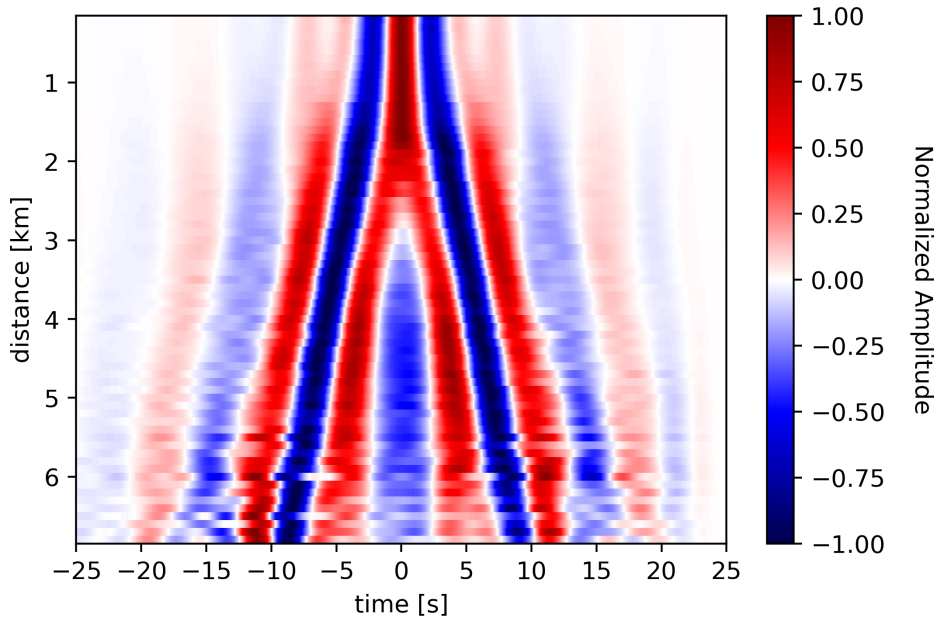

Figure 6: The stacked NCFs. The NCFs are ordered by increasing distance. The Rayleigh wave fundamental mode moveout pattern is clearly observable. The velocity of an individual peak is 1 km/s. The plot has been trimmed to only show lags up to 25 seconds.

The surface wave moveout pattern is clearly visible, and appears to propagate at a similar velocity of the dominant power source observed in the beamforming analysis.

2.3 Automatic Frequency Time Analysis

Further processing is required to extract the dispersion curves from NCFs. This is done using a modified FTAN approach (Dziewonski et al., 1969; Levshin et al., 1972; Levshin & Ritzwoller, 2001) The procedure is well outlined in Bensen et al. (2007). The procedure will be described in the following section in the interest of completeness. The first step is

to convert the data into the frequency domain using the Fourier transform:

$$S(\omega)\int_{-\infty}^{\infty} s(t)e^{i\omega t}dt \tag{4}$$

where $s(t)$ denotes the original signal and $S(\omega)$ denotes the spectrum of the original signal. Once in the frequency domain, a series of Gaussian filters is applied to the spectrum of the original signal. This allows for the spectrum of the signal to be defined as a function of frequency and the center frequency of the Gaussian filter. This is as defined below:

$$S(\omega,\omega_0) = S(\omega)\cdot e^{-\alpha\left(\frac{\omega-\omega_0}{\omega_0}\right)^2} \tag{5}$$

The analytic signal can then be recovered by removing the spectral amplitudes corresponding to negative frequencies and multiplying the remaining signal by two:

$$S_a(\omega,\omega_0) = S(\omega,\omega_0)(1+sgn(\omega)) \tag{6}$$

For each value of ω_0, a separate analytic signal is computed. Each bandpassed analytic signal may then be inverse transformed. Each of these signals will be complex valued. Taking the absolute value of the time domain analytic signal yields the envelope of the original signal. This can then be represented as a 2-D function of frequency and time, as illustrated in Figure 7. Velocity can be calculated by dividing the inter-station distance, and period may be calculated by taking the reciprocal of the frequency.

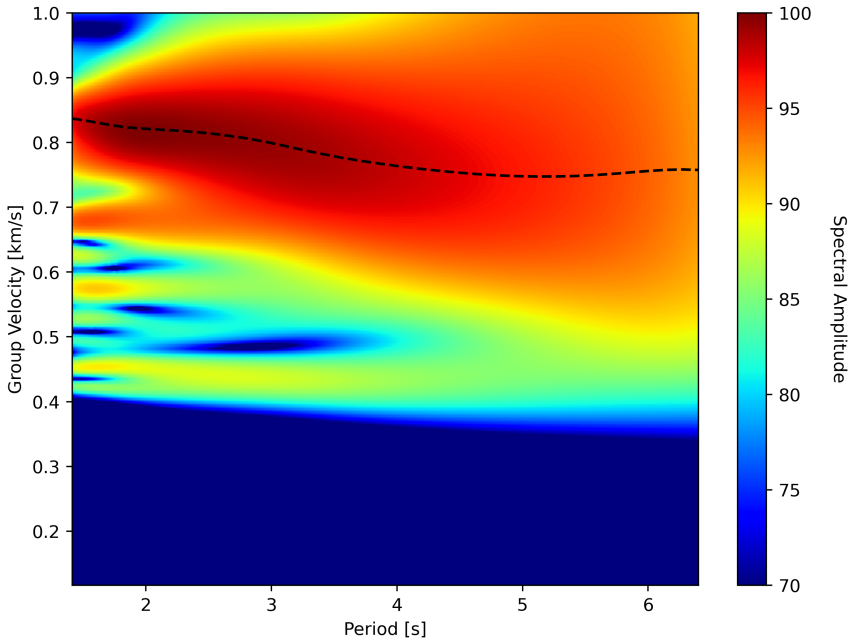

Figure 7: The frequency-time diagram and measured group velocity produced using the Automatic Frequency Time Analysis algorithm. The phase velocity can then be derived from the group velocity.

The group velocity can then be extracted by picking the maximum amplitude of the frequency-time diagram. In order to improve the signal-to-noise ratio of the group velocity measurements, a phase matched filter may be applied to the NCF. This essentially compresses the envelope of the original signal. In the interest of completeness I outline the steps described in Levshin & Ritzwoller (2001). The dispersive surface wave signal may be represented as:

$$S(t) = \frac{1}{\pi}\mathbb{R}\left[\int_{\omega_0}^{\omega_1} |S(\omega)|\, e^{i(\omega t - \Psi(\omega))}\right] d\omega \tag{7}$$

Here, $S(t)$ represents the surface wave signal, $S(\omega)$ is the amplitude spectrum of the surface wave signal, and $\Psi(\omega)$ is some factor controlling the dispersion of the signal. The factor $\Psi(\omega)$ can be approximated as:

$$\Psi(\omega) \simeq \psi(\omega) = k(\omega)\Delta \tag{8}$$

where $k(\omega)$ is the wavenumber as a function of frequency and Δ is the epicentral distance. Given an estimated group velocity curve for the region of interest, $k(\omega)$ can be approximated as:

$$k(\omega) = \int_0^{\omega_0} \frac{d\omega'}{U(\omega')} + \int_{\omega_0}^{\omega} \frac{d\omega'}{U(\omega')} \tag{9}$$

where $U(\omega')$ is the estimated group velocity dispersion curve. An undispersed signal can then be produced using:

$$S_u(t) = \frac{1}{\pi}\mathbb{R}\left[\int_{\omega_0}^{\omega_1} |S(\omega)|\, e^{i(\omega t - \Psi(\omega) + \psi(\omega))} d\omega\right] \tag{10}$$

The envelope of the signal is given by:

$$E(t) = \frac{1}{\pi}\left|\int_{\omega_0}^{\omega_1} |S(\omega)|\, e^{i(\omega t - \Psi(\omega) + \psi(\omega))} d\omega\right| \tag{11}$$

Noise may then be removed by attenuating this envelope function outside of a certain time period. The compressed and attenuated signal is then uncompressed and returned to the time domain. This removes noise that isn't associated with dispersive surface waves. This cleaned signal can be used to create a frequency-time diagram, following the same steps

for the uncleaned signal. The cleaned dispersion curve was used for further analysis in this case. From Figures 8 and 9, it appears that the phase velocity measurements tend to have higher quality. Because of this, only phase velocity dispersion curves were used for further analysis.

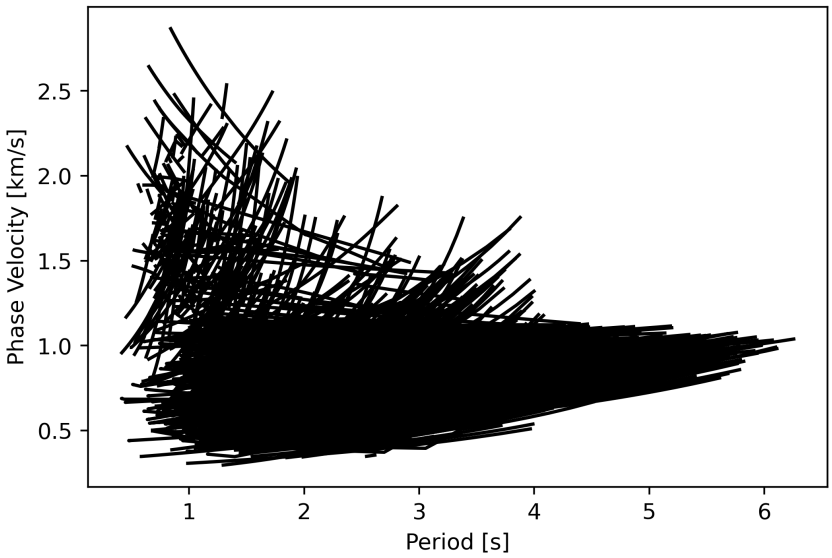

Figure 8: A plot of all the phase velocity measurements.

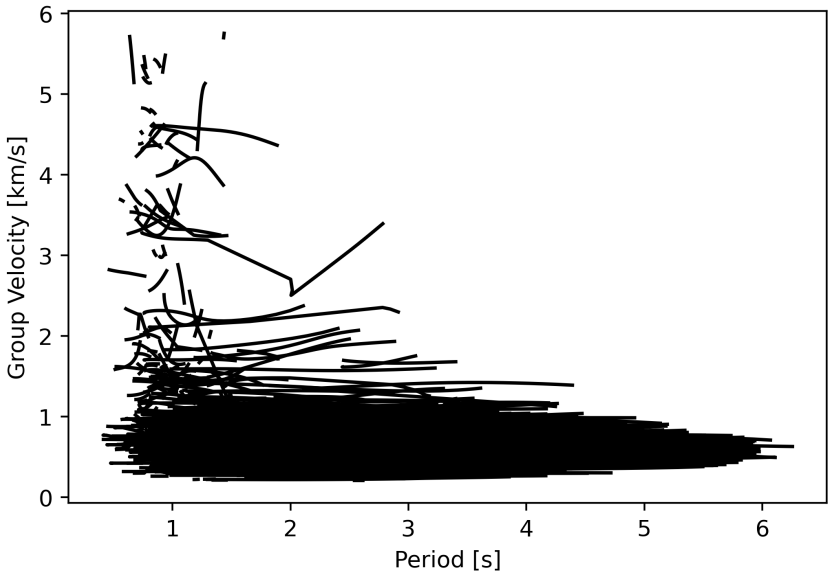

Figure 9: A plot of all the group velocity measurements.

In order to ensure that the automatic measurements are of high quality, several quality control measures were taken. Only dispersion measurements with a signal-to-noise ratio greater than 8 dB were used. Luo et al. (2005) have shown that dispersion measurements with an inter-station distance less than one wavelength tend to be poor quality. Thus, we have removed measurements with an inter-station distance less than one wavelength. The code used for AFTAN in this thesis is available at https://github.com/NoiseCIEI/AFTAN

2.4 Inversion

The inversion scheme used for this thesis is the wavelet based, sparsity constrained method of Fang et al. (2015). The raypath travel time is calculated using the Fast Marching Method

(FMM) of Rawlinson & Sambridge (2005). Some examples of the raypaths calculated using the FMM are shown in Figure 10.

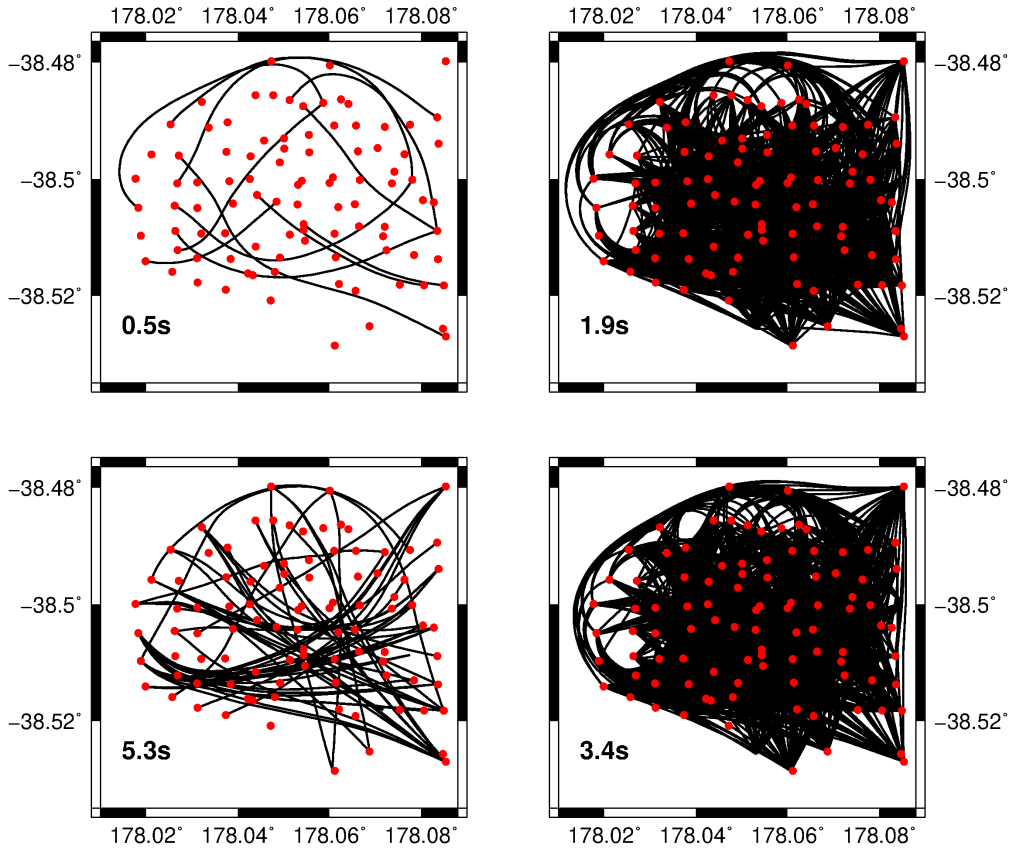

Figure 10: A plot of the ray paths calculated using the Fast Marching Method. The ray paths for several periods are shown. Red dots represent the geophone stations.

One may naively assume that surface waves propagate in straight lines across the study

area. The forward problem may then be expressed as:

$$t_{AB}(\omega) = S_{AB}(\omega) \cdot d_{AB} \tag{12}$$

where t_{AB} is the travel time between station A and station B. The variables d_{AB} and $S_{AB}(\omega)$ represent the straight line distance and slowness along the path between the stations, respectively. However, the velocities of the subsurface are heterogeneous. Due to Fermat's principle of minimum travel time, this may cause significant deviations of the ray path from the assumed straight line. The forward problem is better poised as:

$$t_{AB}(\omega) = \sum_{p=1}^{P} S_p(\omega) \Delta l_{AB} \tag{13}$$

where Δl_{AB} represents the path segment from A to B, and $S_p(\omega)$ is the phase slowness along the path segment, and P is the total number of path segments. A 2-D map of phase velocities may be constructed, such that:

$$S_p(\omega) = \sum_{k=1}^{K} v_{pk} \widehat{S}_k(\omega) \tag{14}$$

where v_{pk} represents the coefficients for the bilinear interpolation between each of the four surrounding grid points, and $\widehat{S}_k(\omega)$ represents the phase slowness at the k$^{\text{th}}$ grid point, which is computed from a 1-D model of shear wave velocities. The slowness is computed using the method of Haskell (1953), with modifications by Dunkin (1965) and Herrmann

(2013). For each observed ray path in the model, the data residual may be calculated as:

$$\delta t_i(\omega) \simeq -\sum_{k=1}^{K} v_{ik} \frac{\delta C_k(\omega)}{C_k^2(\omega)} \tag{15}$$

where the summation over K represents calculating the differential travel time of each segment along the path. The parameter $\delta C_k(\omega)$ is given as:

$$\begin{aligned} \delta C_k(\omega) = \int \Bigg[& \frac{\partial C_k(\omega)}{\partial \alpha_k(z)}\bigg|_{\theta_k} \delta\alpha_k(z) + \frac{\partial C_k(\omega)}{\partial \beta_k(z)}\bigg|_{\theta_k} \delta\beta_k(z) \\ & + \frac{\partial C_k(\omega)}{\partial \rho_k(z)}\bigg|_{\theta_k} \delta\rho_k(z) \Bigg] dz \end{aligned} \tag{16}$$

where $\alpha_k(z)$ is the compressional wave velocity as a function of depth, $\beta_k(z)$ is the shear wave velocity as a function of depth, and $\rho_k(z)$ is density as a function of depth. Surface waves are mainly sensitive to shear wave velocity, so the final model should be a function of the shear wave velocity. Compressional wave velocity and density can all be determined from the shear wave velocity via empirical relations. Applying the empirical relations derived by Brocher (2005), discretizing equation 16, and substituting into equation 15 yields:

$$\begin{aligned} \delta t_i(\omega) = \sum_{k=1}^{K} \left(-\frac{v_{ik}}{C_k^2(\omega)} \right) \sum_{j=1}^{J} \Bigg[& R\alpha(z_j) \frac{\partial C_k(\omega)}{\partial \alpha_k(z_j)} + \frac{\partial C_k(\omega)}{\partial \beta_k(z_j)} \\ & + R_\rho(z_j) \frac{\partial C_k(\omega)}{\partial \rho_k(z_j)} \Bigg]_{\theta_k} \delta\beta_k(z_j) \end{aligned} \tag{17}$$

Note that R_α and R_β are the coefficients from Brocher (2005) to convert from shear wave velocity to the respective parameters. The partial derivatives in equation 17 can be cal-

culated by perturbing the shear wave velocity of the 3-D model at the corresponding grid point, and then performing the forward calculation to determine the resulting perturbation in the phase velocity, as shown in Figure 11.

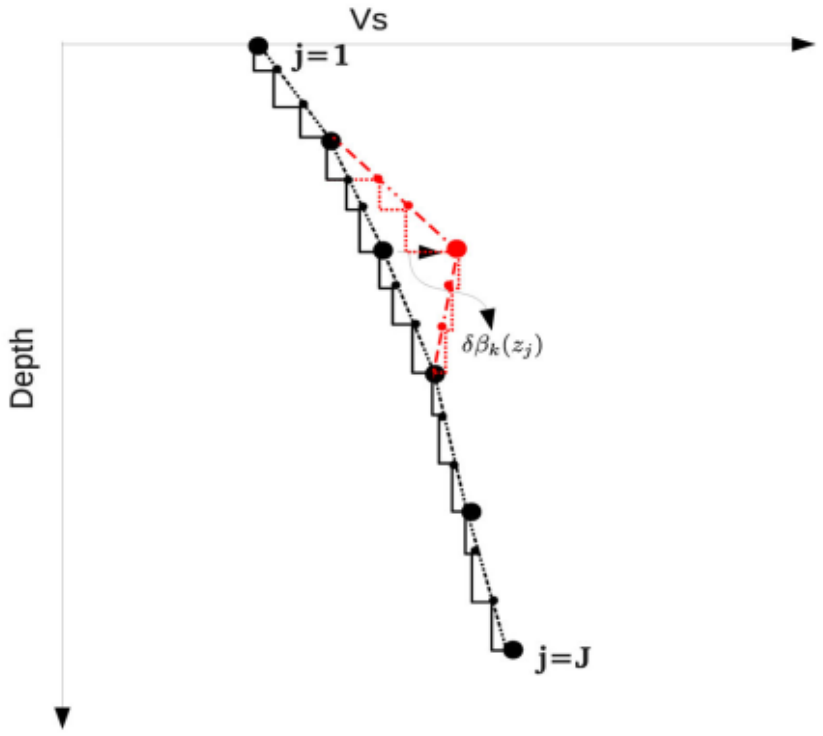

Figure 11: A visualization of the perturbation used to calculate the partial derivatives in Equation 17. Adapted from Fang et al. (2015).

Equation 17 can be written in matrix form as:

$$\mathbf{d} = \mathbf{Gm} \tag{18}$$

In this case **d** is the residual of the travel time from equation 17, **G** is the sensitivity of

the data to the model, and **m** is the model vector. This problem is solved using a wavelet-based sparsity-constrained method (Fang & Zhang, 2014). Solving this problem consists of minimizing the following:

$$\left|\left|\widehat{G}\widehat{m} - d\right|\right|_1 \tag{19}$$

where the hats represent the wavelet transform of the variable. Note that the subscript 1 denotes that the L1-norm is used. In order to stabilize the inversion, a regularization term is added:

$$\left|\left|\widehat{G}\widehat{m} - d\right|\right|_1 + \lambda \, ||\widehat{m}||_1 \tag{20}$$

The parameter λ controls the balance between data misfit and sparsity. Equation 20 may be rewritten in matrix form as:

$$\left|\left|\begin{bmatrix} \widehat{G} \\ \lambda \mathbf{I} \end{bmatrix} \widehat{m} - \begin{bmatrix} d \\ 0 \end{bmatrix}\right|\right|_1 \tag{21}$$

In this case, the data residual may be expressed as:

$$\mathbf{r} = \tilde{\mathbf{G}}\widehat{\mathbf{m}} - \tilde{\mathbf{d}} \tag{22}$$

where the bold characters denote that the variable is in matrix form, $\tilde{\mathbf{G}}$ represents the first term from equation 21, and $\tilde{\mathbf{d}}$ represents the term after the minus sign in equation 21. In

this scheme, the L-1 norm of $\mathbf{r}$ is minimised. The L-1 norm of the residual is denoted as:

$$f(\widehat{\mathbf{m}}) = ||\mathbf{r}||_1 \tag{23}$$

The gradient of the L-1 norm of the residual is:

$$\nabla f(\widehat{\mathbf{m}}) \simeq \tilde{\mathbf{G}}^T \mathbf{R}(\tilde{\mathbf{G}}\widehat{\mathbf{m}} - \tilde{\mathbf{d}}) \tag{24}$$

$\mathbf{R}$ is a diagonal weighting matrix, where the weights are the inverse of the residuals. If a residual is smaller than some predefined threshold, the residual is set to the threshold. In this case the threshold was set to $1x10^{-6}$. Setting the gradient of the L-1 norm to zero yields the following relation:

$$\tilde{\mathbf{G}}^T \mathbf{R}\tilde{\mathbf{G}}\widehat{\mathbf{m}} = \tilde{\mathbf{G}}^T \mathbf{R}\tilde{\mathbf{d}} \tag{25}$$

This problem may be solved using the general least-squares algorithm. However $\tilde{\mathbf{G}}$ is likely to be too large and sparse to be solved with the general least-squares algorithm. In this case the iterative least squares algorithm (LSQR) of Paige & Saunders (1982) may be more suitable. LSQR is used for this inversion methodology. In order to estimate a 1-D model for the area, the average dispersion curve was calculated. A 1-D shear wave velocity model was estimated by dividing the phase velocity by 0.92 to estimate the shear wave velocity. This is because for a uniform half-space with a Poisson's ratio of 0.25, the shear wave velocity is exactly the Rayleigh wave velocity divided by 0.92 (Shearer, 2009). The wavelength was multiplied by 0.63 to estimate the depth at which a given shear wave

velocity corresponds to. The modelling results of Xia et al. (1999) show that multiplying the wavelength corresponding to a Rayleigh wave velocity measurement by a factor of 0.63 roughly estimates the depth at which the Rayleigh wave velocity is sensitive to. The resulting velocity model is shown below (Figure 12).

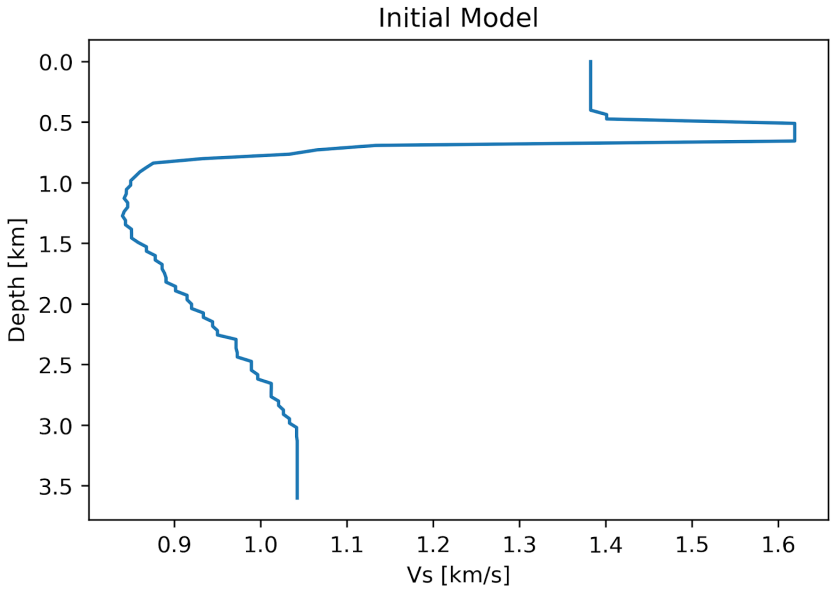

Figure 12: A plot of the initial model, based off of the average Rayleigh wave phase velocity dispersion curve. The approximations in Shearer (2009) and Xia et al. (1999) are used to estimate shear wave velocity and depth, respectively. Next neighbour interpolation was used.

All Rayleigh wave phase velocity measurements were used for the inversion. A 36 by 36 by 14 node grid was used. The spacing of the grid was 0.002° longitude and 0.003° latitude. The depth nodes were located at 0.0, 0.4, 0.6, 0.8, 1.0, 1.2, 1.4, 1.6, 1.8, 2.0, 2.4, 2.8, 3.2, and 3.6 km. A weight parameter of 3.0 was used, and a damping parameter of 1.0 was used. These parameters were decided upon after a process of trial and error. Fang et

al. (2015) recommend that the initial parameter be chosen such that the absolute maximum of the velocity change after the first iteration was approximately 0.4 km/s. The minimum and maximum velocity variation after the first iteration observed for this inversion were -1.3225 and 0.4936 km/s, respectively. It was apparent that the inversion had stabilized after the second iteration, so five iterations were used to ensure that the inversion was stable. The sensitivity of the final model to shear wave velocity at depth is dependent on two main factors. This first is that the density of ray paths is dependent on the period of the measurements. In this experiment, there was good raypath coverage between 0.5 and 5.3 seconds (Figure 10). The other factor is that the sensitivity of surface wave dispersion measurements is dependent on period (Figure 13).

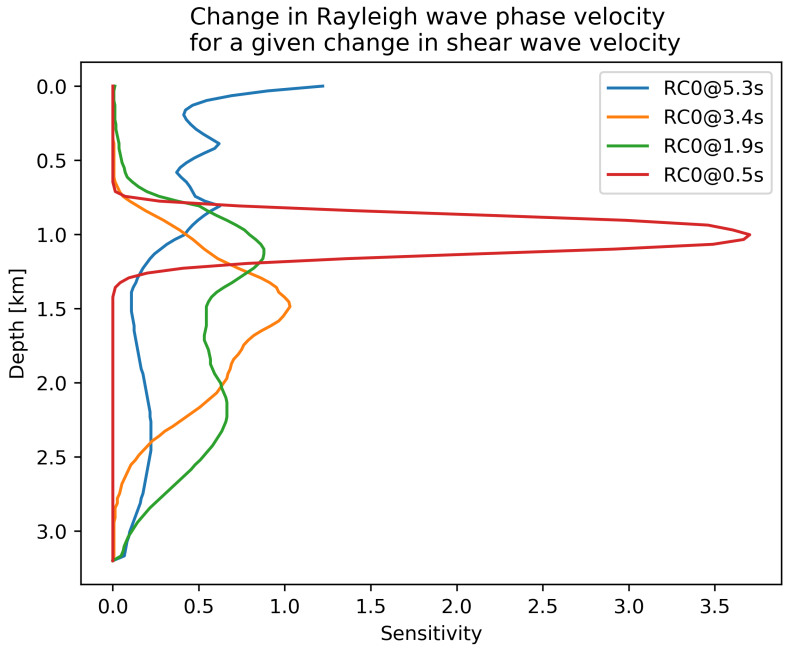

Figure 13: A plot of the sensitivity of Rayleigh wave phase velocity at different periods and depths. The sensitivity is essentially the change in surface wave velocity for a given change in the shear wave velocity at a given depth. Note that the Rayleigh wave phase velocity is strongly dependent on period.

In order to estimate the resolution of the final inversion, a synthetic test was performed. This consisted of prescribing an initial model, and performing the forward calculation to estimate synthetic observations for this model. A 2-D checkerboard pattern was prescribed for each depth node. While there are known issues with the synthetic checkerboard test (Rawlinson & Spakman, 2016), it is generally accepted by the seismic tomography research community that the synthetic checkerboard test provides useful information on the spatial distribution of data resolution. The results of the synthetic checkerboard test for the WVA are shown in Figure 14.

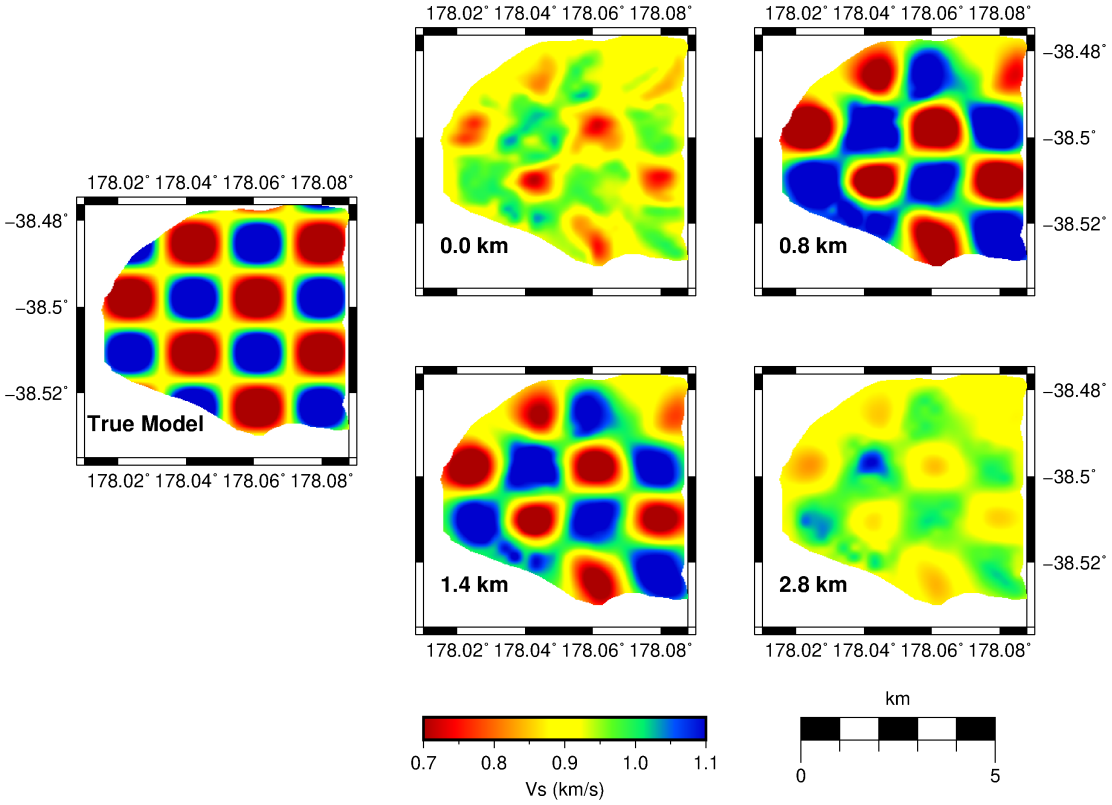

Figure 14: A plot of the synthetic test. Depth is given in the lower left corner of each plot.

The synthetic test shows that the synthetic model is well recovered at intermediate depths, but not as well recovered at greater depths (Figure 14). Note that even at shallow and deep depths, the overall pattern of the true model is recovered, but the amplitude of the checkerboards is not.

3 Results

Rayleigh wave phase velocity measurements made from NCFs were inverted for a 3-D shear wave velocity model. The root mean square of the residuals calculated from the initial model (Figure 12) was 1.300 seconds. As one can see from Table 1, there are minimal changes in the residual after three iterations. This shows that the inversion has stabilized, and that five iterations of inversions is more than enough.

Table 1: Statistics of each inversion iteration.

Iteration #	RMS[a]	Mean[b]	Min. vel. variation[c]	Max. vel. variation[d]
1	1.300	822.5	-1.3552	0.4936
2	0.884	-338.7	-0.0590	0.2661
3	0.758	-71.7	-0.0781	0.0996
4	0.751	-35.2	-0.0240	0.0032
5	0.750	-35.7	-0.0463	0.0654

[a]Root Mean Square of the residuals. Units of seconds.
[b]Mean of the residuals. Units of milliseconds
[c]Minimum Velocity Variation of the model in the inversion. Units of kilometers per second.
[d]Maximum Velocity Variation of the model in the inversion. Units of kilometers per second.

The reduction of the RMS of the residuals from 1.3 to 0.75 seconds shows that the inversion is successfully creating a model that is more consistent with the observed data.

3.1 Model Horizontal Depth Slices

The final model has several interesting features that are apparent in the horizontal cross-sections (Figure 15). Low-velocity zones are apparent near the surface expressions of both

the 1930 and 2018 eruption. The shape of these low-velocity zones vary with depth. The low-velocity zones appear to be connected or nearly connected at 0.8 km and 2.8 km depth. There appears to be a distinct gap between the low-velocity zones at a depth of 1.4 km. At the surface, there appear to be several areas of low-velocity, scattered throughout the study area. These low-velocity zones correspond to the previously known eruptions, as well as areas of known mud bubbling (Ridd, 1970).

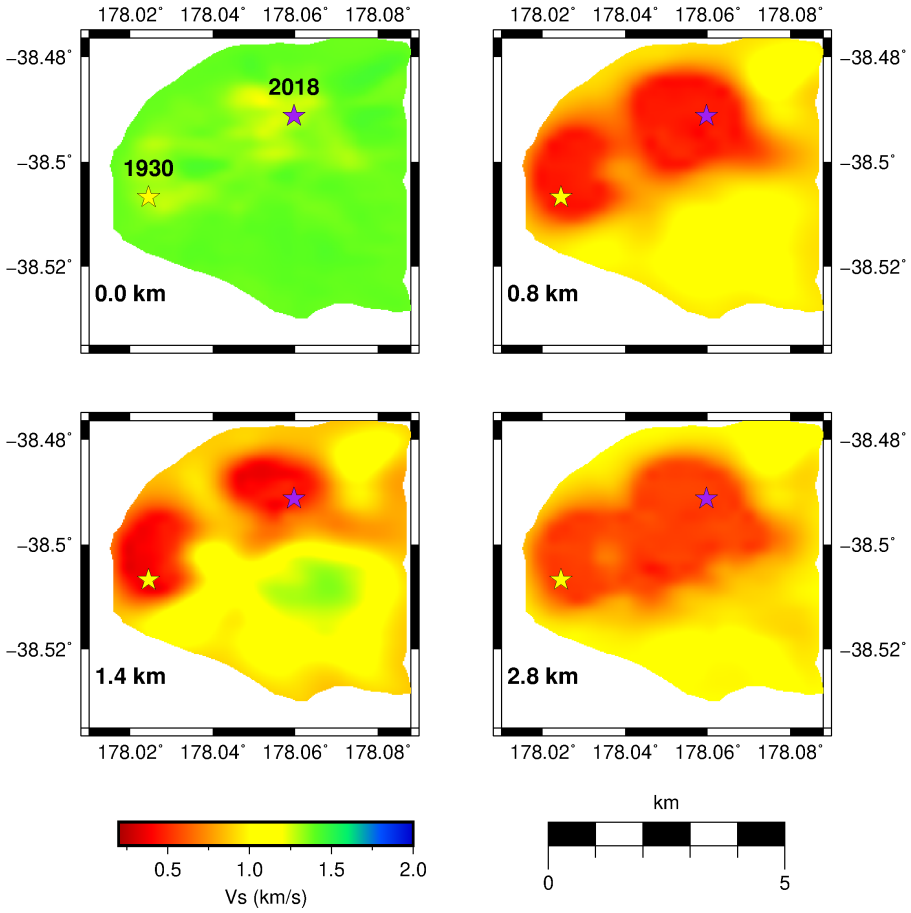

Figure 15: A plot of horizontal slices of the final 3-D model. Depth is shown in the lower left corner. Areas outside of the Waimata Valley Array are masked out. The yellow star represents the surface expression of the 1930 eruption, and the purple star represents the surface expression of the 2018 eruption.

A distinctive kidney shape is observed in the low-velocity zone corresponding to the 1930 eruption. It appears that a low point in the surface topography may be related to this low-velocity zone (Figure 16).

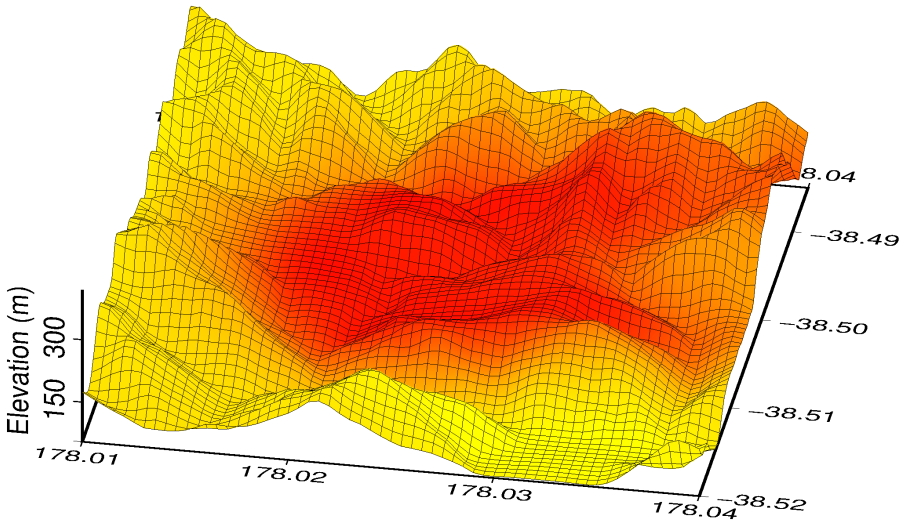

Figure 16: A plot of seismic velocities in the region of the 1930 eruption, overlain on surface elevation. The seismic velocity slice was taken from 0.8 km depth.

3.2 Model Vertical Cross-Section

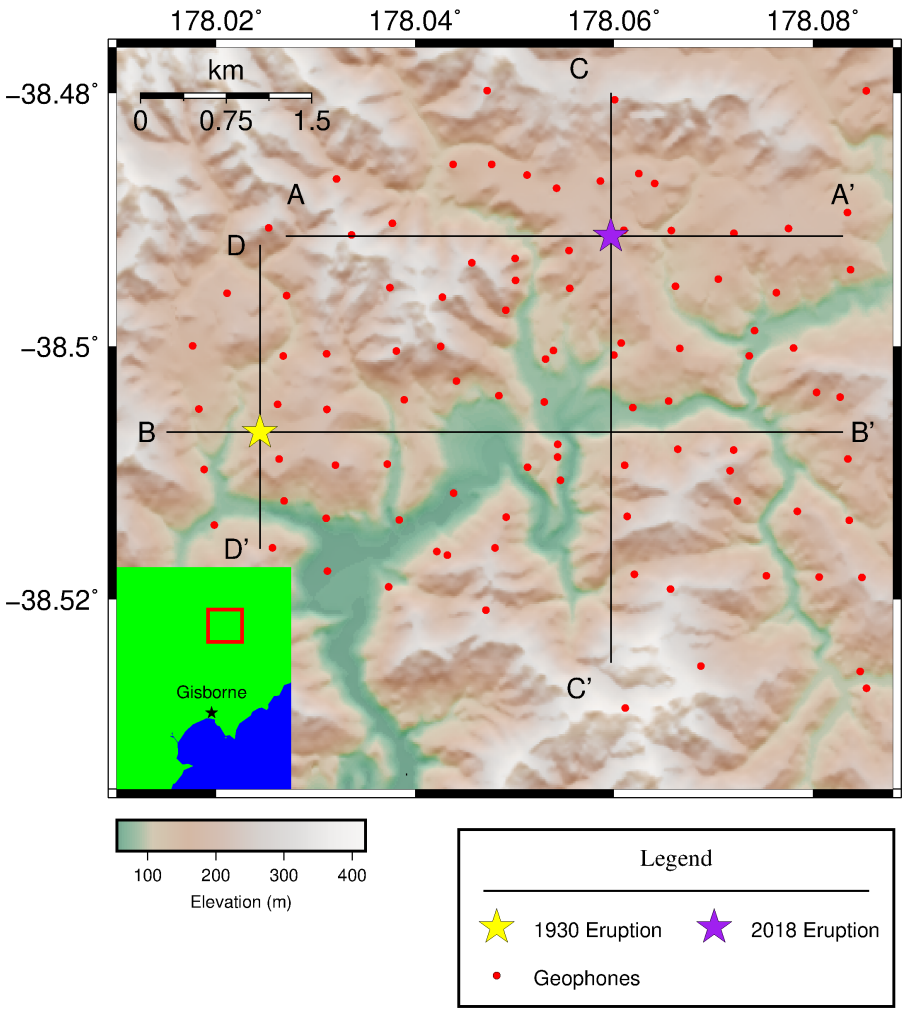

Figure 17: A plot of the study area, with cross-section profiles indicated by thin black lines.

Vertical cross-sections through the model (Figure 18) show that the south-east corner of the study area has a much higher seismic velocity than the rest of the surface area. It

is likely that the higher velocity material consists of deposited sediments, while the low-velocity material is likely to be mud that has risen diapirically in association with the observed mud volcanism at the surface.

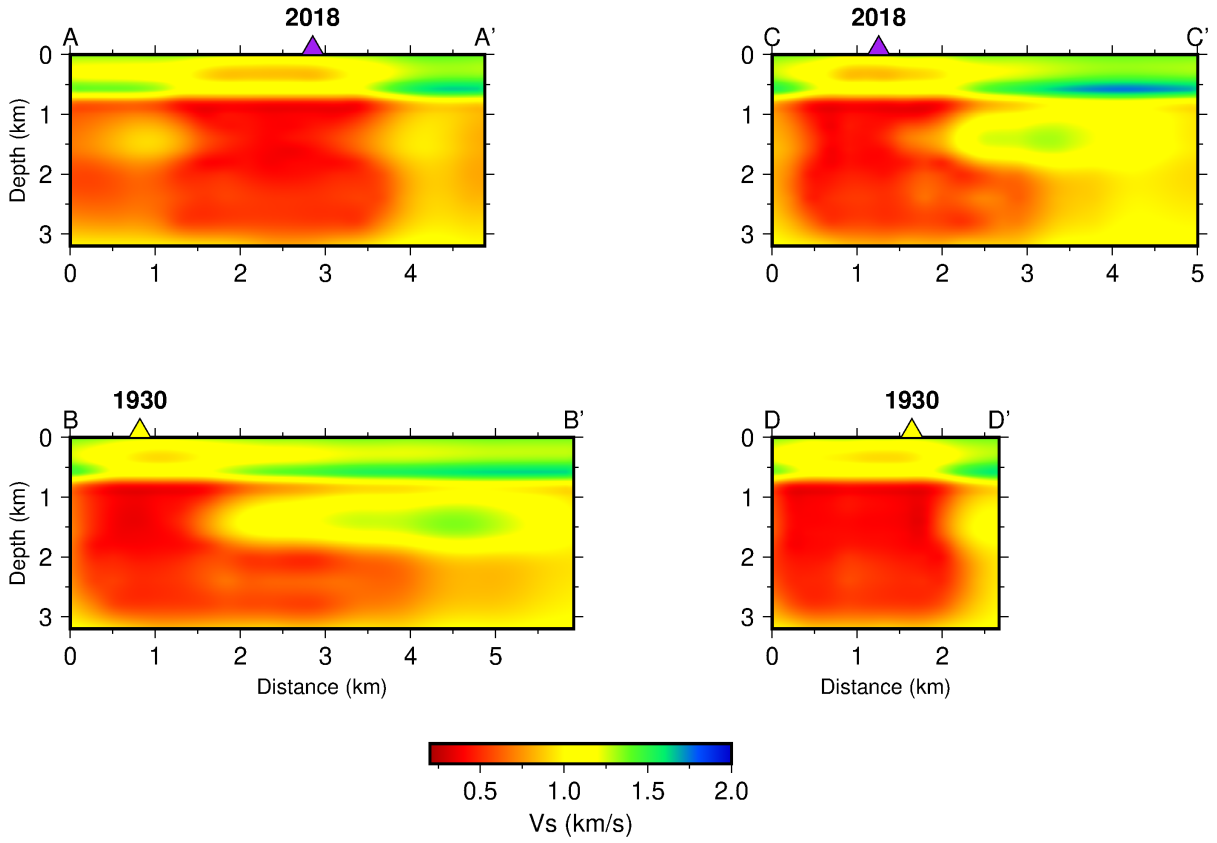

Figure 18: Vertical cross-sections of the 3-D model. Cross-sections correspond to Figure 17. The left column of cross-sections show west to east cross-sections, while the right column represents north to south cross-sections. Eruptions are depicted by coloured triangles.

The low-velocity zones appear to be roughly cylindrical in areas underlying the surface

expressions of both mud volcanoes. The widths of the low-velocity zones appear to be slightly larger than one kilometer. This represents a very large volume of mud.

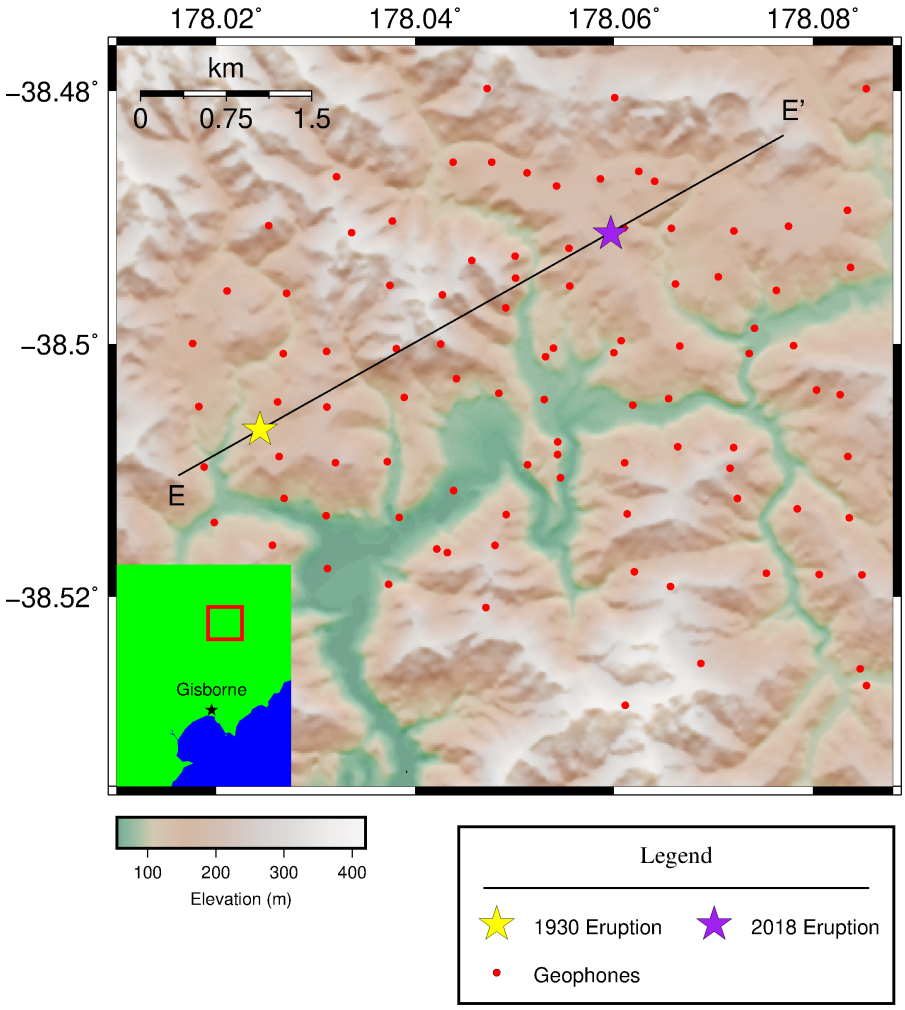

Figure 19: Plot of the study area, with the cross-section between the two eruption sites.

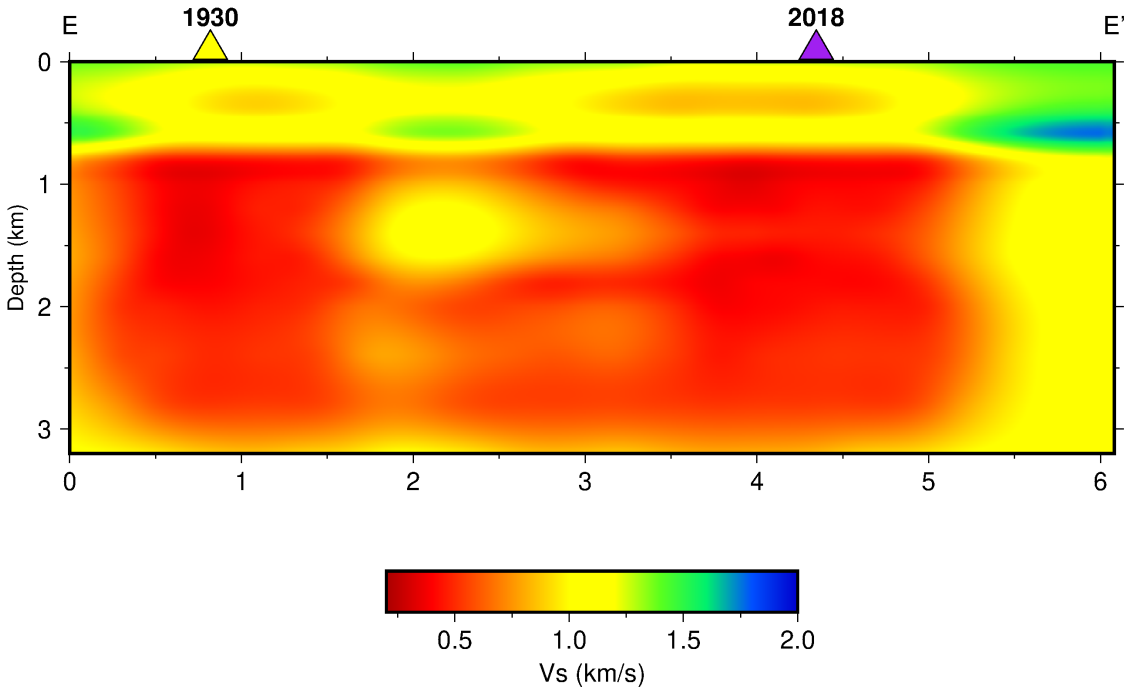

Figure 20: A plot of the cross-section depicted in Figure 19.

Significant structure is visible in the vertical cross-section between both eruption sites (Figure 20). Several layers of low seismic velocities are apparent. These layers appear to connect both of the low-velocity zones underlying the surface expressions of the ruptures. It appears in Figure 20 that the low-velocity only extends to a depth of 3 km. This is likely to be an artifact, as the inversion is not very sensitive to deeper depths.

In order to check if the station elevations had any effect on the results of the 3-D model, a plot was made of the station elevations overlaying a horizontal slice of the 3-D model (Figure 21). No discernible correlation between the station elevations and the results of the 3-D model was found. This suggests that station elevation corrections are not required

for the model.

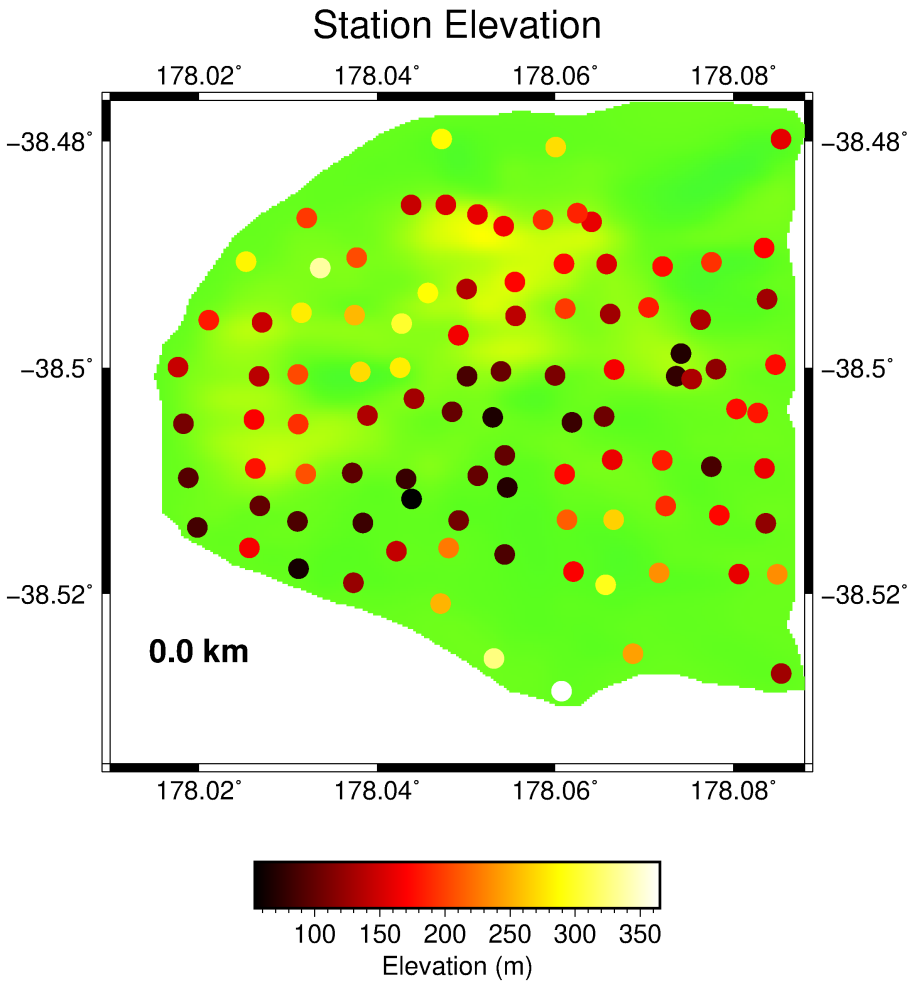

Figure 21: A plot of the geophone stations coloured by elevation overlaid on the seismic velocity model for 0 km depth (See Figure 15 for velocity scale).

4 Discussion

In this study, a dense array of 97 short-period geophones was used to derive a high resolution 3-D shear wave model of the shallow subsurface in a region of known mud volcanoes: the Waimata Valley, New Zealand. NCFs were calculated between the vertical components of each pair of geophones. Rayleigh wave phase velocities between pairs of geophones were calculated using AFTAN. These Rayleigh wave phase velocity measurements were then inverted to recover a 3-D shear wave velocity model from 0 to 3.2 km depth.

The background seismic noise field appears to be suitable for ANT. Using beamforming analysis, there was found to be a strong noise signal coming from all directions (Figure 4). The dominant power was found to be coming from the south-east. This preferential directivity of the background noise is likely to bias the NCFs. When viewing the stacked NCFs with distance (Figure 6), both the causal and acausal sides appear to be relatively symmetric. This suggests that the bias is not overly large.

The results of the dispersion curve measurements appear to be of high quality. There appear to be a few erroneous measurements in the group velocity curve (Figure 9), characterized by a sharp change in velocity. The phase velocity measurements appear to be of higher quality (Figure 8). Significant variation is observed among the phase velocity curves. This suggests that there is strong heterogeneity throughout the study area. Based on the initial velocity model (Figure 12), derived from the average phase velocity curve, there appears to be a low-velocity zone in the study area. This suggests that the reservoir of the mud volcano may be distributed over much of the study area. Note that the transition to low-velocity at 0.7 km depth appears to be very sharp in the initial model.

The results of the synthetic tests show that high-resolution tomography is possible with

this dataset. The prescribed seismic velocity anomalies of the checkerboard test are recovered well at intermediate depths, while only the broad pattern of the checkers is recovered at shallow and deep depths (Figure 14). The amplitude of the checkers is not well recovered at shallow and deep depths, due to the lack of sensitivity of the measurements to these depths. Because the initial checkerboard model is not very similar to the velocities of the model observed in the actual inversion, it is likely that the resolution of the actual model differs from that of the synthetic model.

It appears that significant heterogeneities are recovered by the inversion of the real data. There are low-velocity zones that underlie each of the 1930 and 2018 eruption surface expressions, throughout the model depth range. There are significant implications to this. The low-velocity zone underneath the 1930 eruption site shows that the source of the mud volcano persists, even after a long time. This suggests that the mud volcano could erupt again, given the right temperature and pressure conditions. The low-velocity zone underlying the 2018 eruption is a precursory signal of the eruption that occurred 10 months later. Given that the array was decommissioned well before the 2018 eruption, it is striking that such a prominent signal was observed. This suggests that sites of future mud volcano eruptions could be identified well before the eruption. This may give people time to prepare for potential hazards, and in some cases may give enough time to adapt surrounding infrastructure to mitigate future eruptions of the mud volcano.

There is also an interesting feature that is apparent in the vertical cross-sections of the 3-D model (Figures 18 & 20). In addition to the vertical low-velocity zones beneath the eruption sites, there appear to be three main low-velocity layers in the model that connect the eruption sites. The uppermost layer extends from 200-500 m depth, and the next deep-

est layer extends from 800-1000 m in depth. The third layer extends from 1.5-3 km in depth. This bottom layer is relatively thick compared to the other two low-velocity horizontal layers that were observed. There appears to be further structure within this third layer, with another two interfaces being possible at approximately 2 km depth and 2.8 km depth, bounding a low-velocity zone across the region. The insufficient resolution of the model at this depth suggests that a definitive statement on this would be unjustified. Two potential mechanisms could explain the observed triple layer structure. The first hypothesis is that mud may have intruded between weaknesses of the sedimentary layers in a form of diapiric intrusion. This would suggest that the mud volcano reservoirs are connected by subterranean channels of mud. Connections between the two main vertical anomalies are indeed most distinct on the cross-section between the eruption sites (Figure 20). An alternative hypothesis for this triple layered structure is that the layers represent ancient mud volcano eruptions, that have since been overlain by younger sediments. A large eruption of mud at the surface may have extended throughout the study area connecting the two areas of mud volcanism. This would suggest that these mud volcanoes are very old, and that they have erupted many times over the lifetime of the mud volcano. Higher resolution models and anisotropy measurements may be able to shed more light on which hypothesis is more likely to be correct.

5 Conclusions

A high-resolution 3-D model of shear wave velocities was produced for the Waimata Valley, New Zealand. The background noise field recorded by the WVA was found to be suit-

able for ambient noise tomography, with a good azimuthal distribution of noise sources. The resulting 3-D model was found to be a high-resolution image of the subsurface through synthetic tests. Several instances of mud volcanism have been observed near the Waimata Valley. Two low-velocity zones that underlie the surface expression of eruptions in 1930 and 2018 were imaged. This shows that the source of a mud volcano remains long after the mud volcano has erupted. This also suggests that low-velocity zones imaged using ambient noise tomography may be used to predict the sites of future mud volcanism, allowing for the reduction of human impacts due to the eruption of a mud volcano.

6 Future Work

The use of ambient noise to uncover information about the earth offers several promising avenues of future investigation. In order to increase the aperture of the array used for imaging, additional seismic stations could be used to calculate the NCFs. Conveniently, an array of broadband seismometers, known as the Gisborne Array, was deployed during the same time period as the WVA. This array also has the benefits of being in operation for longer, allowing for an increased number of NCFs used in the stacking, as well as being composed of broadband seismometers. These broadband seismometers are more sensitive to longer period oscillations than the short-period geophones used in the WVA. This should allow for higher quality measurements at long periods. Using ambient noise for temporal monitoring has also become a commonly used tool to investigate the subsurface (Jiang & Denolle, 2020; Lecocq et al., 2017). Mud volcanoes may exhibit precursory phenomena in the form of changes in subsurface seismic velocities. This could allow more

insight into the temporal evolution of the mud volcano, and should be readily accessible with the current dataset. As well, making both radial and azimuthal seismic anisotropy measurements may give deeper insight into the formation process of these mud volcanoes. The inversion may be better constrained using a joint inversion of both phase and group velocity.

7 Acknowledgements

I would like to sincerely thank Dr. Adebayo Oluwaseun Ojo for teaching me valuable information about ambient noise tomography. I wouldn't have been able to complete this project without his assistance. I would also like to thank Drs. Honn Kao and Lucinda Leonard. I appreciate you taking on this project along with me, and I greatly benefited from your expertise, knowledge, and advice throughout this project. I am grateful that Dr. Hongjian Fang provided the DSurfTomo code openly, as well as Dr. Fang's assistance regarding the use of the code. I am thankful that Dr. Rebecca Bell shared the Waimata Valley Array data, especially given the difficult pandemic conditions that Dr. Bell had to deal with when delivering the data. This project would have been impossible without the dataset provided by Dr. Bell. Dr. Hongyu Yu began the conversion of the dataset from GIPP to miniSEED format. This initial start helped me to get the project going quickly. I would also like to thank the rest of the PGC seismology group for their constructive comments. Some figures were produced with the Generic Mapping Tool (Wessel et al., 2013). Elevation data from Columbus (2011) was used. Lastly, I would like to thank my family and friends for their support throughout this project.

References

Barmin, M., Ritzwoller, M., & Levshin, A. (2001). A fast and reliable method for surface wave tomography. In *Monitoring the comprehensive nuclear-test-ban treaty: Surface waves* (p. 1351–1375). Birkhäuser, Basel. doi: 10.1007/978-3-0348-8264-4_3

Bell, R., Gray, M., Morgan, J., Warner, M., Watkins, S., Lacey, H., Fagereng, A., McNeill, L., Jacobs, K., Henrys, S., Fry, B., Black, J., Lane, V., Daly, D., Lindsay, D., & Bangs, N. (2019). *New Zealand 3D full waveform inversion (NZ3D-FWI) 2017-2018 field acquisition report* (Tech. Rep.). Lower Hutt, N.Z.. doi: 10.21420/ZZ8R-QR04

Bensen, G., Ritzwoller, M., Barmin, M., Levshin, A., Lin, F., Moschetti, M., Shapiro, N., & Yang, Y. (2007). Processing seismic ambient noise data to obtain reliable broad-band surface wave dispersion measurements. *Geophysical Journal International*, *169*(3), 1239–1260. doi: 10.1111/j.1365-246X.2007.03374.x

Brocher, T. (2005). Empirical relations between elastic wavespeeds and density in the earth's crust. *Bulletin of the Seismological Society of America*, *95*(6), 2081–2092. doi: 10.1785/0120050077

Clark, K., Howarth, J., Litchfield, N., Cochran, U., Turnbull, J., Dowling, L., Howell, A., Berryman, K., & Wolfe, F. (2019). Geological evidence for past large earthquakes and tsunamis along the Hikurangi subduction margin, New Zealand. *Marine Geology*, *412*, 139–172. doi: 10.1016/j.margeo.2019.03.004

Columbus, J., Sirguey, P., & Tenzer, R. (2011). A free fully assessed 15 metre digital elevation model for New Zealand. *Survey Quarterly*, *300*(66), 16.

Dalcín, L., Paz, R., & Storti, M. (2005). MPI for Python. *Journal of Parallel and Distributed Computing*, *65*(9), 1108–1115. doi: 10.1016/j.jpdc.2005.03.010

Drake, P. (2020). Comment to "More than ten years of Lusi: A review of facts, coincidences, and past and future studies" by Miller and Mazzini (2018): Taking the trigger debate above ground. *Marine and Petroleum Geology*, *113*. doi: 10.1016/j.marpetgeo.2019.104079

Dunkin, J. (1965). Computation of modal solutions in layered, elastic media at high frequencies. *Bulletin of the Seismological Society of America*, *55*(2), 335–358.

Dziewonski, A., Bloch, S., & Landisman, M. (1969). A technique for the analysis of transient seismic signals. *Bulletin of the Seismological Society of America*, *59*(1), 427–444.

Evans, R., Davies, R., & Stewart, S. (2007). Internal structure and eruptive history of a kilometre-scale mud volcano system, South Caspian Sea. *Basin Research*, *19*(1), 153–163. doi: 10.1111/j.1365-2117.2007.00315.x

Fang, H., Yao, H., Zhang, H., Huang, Y.-C., & Hilst, R. (2015). Direct inversion of surface wave dispersion for three-dimensional shallow crustal structure based on ray tracing: Methodology and application. *Geophysical Journal International*, *201*(3), 1251–1263. doi: 10.1093/gji/ggv080

Fang, H., & Zhang, H. (2014). Wavelet-based double-difference seismic tomography with sparsity regularization. *Geophysical Journal International*, *199*(2), 944–955. doi: 10.1093/gji/ggu305

Fowler, C. (2005). *The solid earth: An introduction to global geophysics* (2nd ed.). Cambridge, UK: Cambridge University Press.

Ginsburg, G., Milkov, A., Soloviev, V., Egorov, A., Cherkashev, G., Vogt, P., Crane, K., Lorenson, T., & Khutorskoy, M. (1999). Gas hydrate accumulation at the Håkon Mosby Mud Volcano. *Geo-Marine Letters*, *19*(1–2), 57–67. doi: 10.1007/s003670050093

Haskell, N. (1953). The dispersion of surface waves on multilayered media. *Bulletin of the Seismological Society of America*, *43*(1), 17–34.

Haubrich, R., & McCamy, K. (1969). Microseisms: Coastal and pelagic sources. *Reviews of Geophysics*, *7*(3), 539-571. doi: 10.1029/RG007i003p00539

Herrmann, R. B. (2013). Computer programs in seismology: An evolving tool for instruction and research. *Seismological Research Letters*, *84*(6), 1081-1088. doi: 10.1785/0220110096

Hovland, M., Hill, A., & Stokes, D. (1997). The structure and geomorphology of the Dashgil mud volcano, Azerbaijan. *Geomorphology*, *21*(1), 1–15. doi: 10.1016/S0169-555X(97)00034-2

Jiang, C., & Denolle, M. (2020). NoisePy: A new high-performance Python tool for ambient-noise seismology. *Seismological Research Letters*, *91*(3), 1853-1866. doi: 10.1785/0220190364

Katz, H., & Wood, R. (1980). Submerged margin east of the North Island, New Zealand, and its petroleum potential. In *Symposium of petroleum potential in the island arcs,*

small ocean basins, submerged margins and related areas (p. 221–235). Wellington, NZ: United Nations Economic and Social Commission for Asia and the Far East.

King, D., Shaw, W., Meihana, P., & Goff, J. (2018). Māori oral histories and the impact of tsunamis in Aotearoa-New Zealand. *Natural Hazards and Earth System Sciences*, *18*(3), 907–919. doi: 10.5194/nhess-18-907-2018

Kopf, A. (2002). Significance of mud volcanism. *Reviews of Geophysics*, *40*(2), 1005. doi: 10.1029/2000RG000093.

Krischer, L., Smith, J., Lei, W., Lefebvre, M., Ruan, Y., Andrade, E., Podhorszki, N., Bozdağ, E., & Tromp, J. (2016). An adaptable seismic data format. *Geophysical Journal International*, *207*(2), 1003–1011. doi: 10.1093/gji/ggw319

Lecocq, T., Longuevergne, L., Pedersen, H., Brenguier, F., & Stammler, K. (2017). Monitoring ground water storage at mesoscale using seismic noise: 30 years of continuous observation and thermo-elastic and hydrological modeling. *Scientific Reports*, *7*(1), 14241. doi: 10.1038/s41598-017-14468-9

Levshin, A., Pisarenko, V., & Pogrebinsky, G. (1972). On a frequency-time analysis of oscillations. *Annales de geophysique*, *28*(2), 211–218.

Levshin, A., & Ritzwoller, M. (2001). Automated detection, extraction, and measurement of regional surface waves. In *Monitoring the comprehensive nuclear-test-ban treaty: Surface waves.* Birkhäuser, Basel. doi: 10.1007/978-3-0348-8264-4_11

Luo, Y., Yang, Y., Xu, Y., Xu, H., Zhao, K., & Wang, K. (2015). On the limitations of interstation distances in ambient noise tomography. *Geophysical Journal International*, *201*(2), 652–661. doi: 10.1093/gji/ggv043

Milkov, A., Sassen, R., Apanasovich, T., & Dadashev, F. (2003). Global gas flux from mud volcanoes: A significant source of fossil methane in the atmosphere and the ocean. *Geophysical Research Letters*, *30*(2), 1037. doi: 10.1029/2002GL016358

Paige, C., & Saunders, M. (1982). LSQR: An algorithm for sparse linear equations and sparse least squares. *ACM Transactions on Mathematical Software (TOMS*, *8*(1), 43–71.

Rawlinson, N., & Sambridge, M. (2005). The fast marching method: An effective tool for tomographic imaging and tracking multiple phases in complex layered media. *Exploration Geophysics*, *36*(4), 341–350.

Richards, J. (2011). Report into the past present and future social impacts of Lumpur Sidoarjo. *Humanitus Sidoarjo Fund*, 1–162. doi: 10.1071/EG05341

Ridd, M. (1964). Succession and structural interpretation of the Whangara-Waimata area, Gisborne, New Zealand. *New Zealand Journal of Geology and Geophysics*, *7*(2), 279–298. doi: 10.1080/00288306.1964.10420175

Ridd, M. (1970). Mud volcanoes in New Zealand. *AAPG Bulletin*, *54*(4), 601–616. doi: 10.1306/5D25CA19-16C1-11D7-8645000102C1865D.

Rost, S., & Thomas, C. (2002). Array seismology: Methods and applications. *Reviews of Geophysics*, *40*(3), 1008. doi: 10.1029/2000RG000100

Rudolph, M., & Manga, M. (2010). Mud volcano response to the 4 April 2010 El Mayor-Cucapah earthquake. *Journal of Geophysical Research: Solid Earth*, *115*, B12211. doi: 10.1029/2010JB007737

Sabra, K. G., Gerstoft, P., Roux, P., Kuperman, W. A., & Fehler, M. C. (2005). Extracting time-domain Green's function estimates from ambient seismic noise. *Geophysical Research Letters*, *32*(3), L03310. doi: 10.1029/2004GL021862

Sawolo, N., Sutriono, E., Istadi, B., & Darmoyo, A. (2009). The LUSI mud volcano triggering controversy: Was it caused by drilling? *Marine and Petroleum Geology*, *26*(9), 1766–1784. doi: 10.1016/j.marpetgeo.2009.04.002

Schimmel, M., & Paulssen, H. (1997). Noise reduction and detection of weak, coherent signals through phase-weighted stacks. *Geophysical Journal International*, *130*(2), 497–505.

Shapiro, N. M., Campillo, M., Stehly, L., & Ritzwoller, M. H. (2005). High-resolution surface-wave tomography from ambient seismic noise. *Science*, *307*(5715), 1615–1618. doi: 10.1126/science.1108339

Shearer, P. (2009). Introduction to seismology. *Cambridge University Press*, 396. doi: 10.1017/CBO9780511841552

Snieder, R. (2004). Extracting the Green's function from the correlation of coda waves: A derivation based on stationary phase. *Physical Review E*, *69*(4), 046610. doi: 10.1103/PhysRevE.69.046610

Tian, Y., & Ritzwoller, M. (2015). Directionality of ambient noise on the Juan de Fuca plate: Implications for source locations of the primary and secondary microseisms. *Geophysical Journal International*, *201*(1), 429–443. doi: 10.1093/gji/ggv024

Tingay, M., Heidbach, O., Davies, R., & Swarbrick, R. (2008). Triggering of the Lusi mud eruption: Earthquake versus drilling initiation. *Geology*, *36*(8), 63-6429. doi: 10.1130/G24697A.1

Wallace, L., Reyners, M., Cochran, U., Bannister, S., Barnes, P., Berryman, K., Downes, G., Eberhart-Phillips, D., Fagereng, A., Ellis, S., Nicol, A., McCaffrey, R., Beavan, R., Henrys, S., Sutherland, R., Barker, D., Litchfield, N., Townend, J., Robinson, R., ... Power, W. (2009). Characterizing the seismogenic zone of a major plate boundary subduction thrust: Hikurangi Margin, New Zealand. *Geochemistry, Geophysics, Geosystems*, *10*(10), Q10006. doi: 10.1029/2009GC002610

Welch, P. (1967). The use of fast Fourier transform for the estimation of power spectra: A method based on time averaging over short, modified periodograms. *IEEE Transactions on Audio and Electroacoustics*, *15*(2), 70–73. doi: 10.1109/TAU.1967.1161901

Wessel, P., Smith, W. H. F., Scharroo, R., Luis, J., & Wobbe, F. (2013). Generic Mapping Tools: Improved Version Released. *Eos Transactions American Geophysical Union*, *94*(45), 409-410. doi: 10.1002/2013EO450001

Xia, J., Miller, R., & Park, C. (1999). Estimation of near-surface shear-wave velocity by inversion of Rayleigh waves. *Geophysics*, *64*(3), 691–700. doi: 10.1190/1.1444578

Zhang, X., Curtis, A., Galetti, E., & Ridder, S. (2018). 3-D Monte Carlo surface wave tomography. *Geophysical Journal International*, *215*(3), 1644–1658. doi: 10.1093/gji/ggy362